

Supporting Information

Polyoxometalate–Cyclodextrin Metal–Organic Frameworks: From Tunable Structure to Customized Storage Functionality

Peng Yang,[†] Wenli Zhao,[‡] Aleksander Shkurenko,[§] Youssef Belmabkhout,[§] Mohamed Eddaoudi,[§]
Xiaochen Dong,[‡] Husam N. Alshareef,[∇] and Niveen M. Khashab^{†,*}

[†] Smart Hybrid Materials Research Group (SHMs), Advanced Membranes and Porous Materials Center (AMPMC), King Abdullah University of Science and Technology (KAUST), Thuwal 23955, Saudi Arabia.

[‡] School of Physical and Mathematical Sciences, Nanjing Tech University, Nanjing 211800, China.

[§] Functional Materials Design, Discovery and Development Research Group (FMD³), Advanced Membranes and Porous Materials Center (AMPMC), King Abdullah University of Science and Technology (KAUST), Thuwal 23955, Saudi Arabia.

[∇] Materials Sciences and Engineering, Physical Science and Engineering Division, King Abdullah University of Science and Technology (KAUST), Thuwal 23955, Saudi Arabia.

1. Materials and Physical Measurements.

All reagents were purchased from commercial sources and used without further purification. Powder X-ray diffraction (PXRD) patterns were obtained using a Bruker D8 ADVANCE diffractometer with Cu $K\alpha$ radiation ($\lambda = 1.54056 \text{ \AA}$). The FT-IR spectra were recorded on KBr disk using a Nicolet-Avatar 370 spectrometer between 400 and 4000 cm^{-1} . Thermogravimetric analyses were carried out on a TA Instruments SDT Q600 thermobalance with a 100 mL min^{-1} flow of nitrogen; the temperature was ramped from 20 $^{\circ}\text{C}$ to 800 $^{\circ}\text{C}$ at a rate of 5 $^{\circ}\text{C min}^{-1}$. Elemental analyses: CHN microanalyses were performed on a Perkin-Elmer 240C elemental analyser, and ICP-OES analyses were carried out on a PerkinElmer Optima 8300 optical emission spectrometer. The NMR spectra were recorded on a Bruker Avance III 400 MHz instrument at room temperature, using 5 mm tubes for ^1H and ^{13}P with respective resonance frequencies of 399.78 MHz (^1H) and 162.14 MHz (^{13}P). The chemical shifts are reported with respect to the references $\text{Si}(\text{CH}_3)_4$ (^1H) and 85% H_3PO_4 (^{31}P). Scanning electron microscope (Merlin-61-95, ZEISS, Germany) was used to characterize the surface morphology of obtained materials. X-ray photoelectron spectra (XPS) were carried out on a Kratos AXIS Ultra DLD spectrometer with Al $K\alpha$ X-ray source using the C 1s peak at 284.8 eV as an internal standard.

2. Synthesis of $\text{K}_{2.5}\text{Na}_{2.5}[(\text{PW}_{12}\text{O}_{40})(\text{CH}_3\text{COO}\alpha\text{-CD})(\text{OH})]\cdot 19\text{H}_2\text{O}$ (POT-CD)

To a solution of α -cyclodextrin (0.097 g, 0.100 mmol) in 5 mL 1 M $\text{KCH}_3\text{COO}/\text{CH}_3\text{COOH}$ buffer (pH 5.0), 85% H_3PO_4 (20 μL) and $\text{Na}_2\text{WO}_4\cdot 2\text{H}_2\text{O}$ (0.330 g, 1.000 mmol) were added successively upon stirring. The solution was then stirred for 1 hour at 80 $^{\circ}\text{C}$. The turbid white solution was cooled to room temperature, filtered, and the filtrate was allowed to evaporate in an open vial at room temperature. The block-shaped colorless crystalline product **POT-CD** started to appear after one week and was collected by filtration and air-dried. Yield: 0.295 g (80 % based on W). Elemental analysis (%): Calcd: K 2.21, Na 1.30, P 0.70, W 49.87, C 10.32; Found: K 1.92, Na 1.15, P 0.70, W 49.16, C 10.42. IR (2% KBr pellet, v/cm^{-1}): 2935 (w), 1635 (s), 1411 (w), 1369 (w), 1338 (w), 1284 (w), 1238 (w), 1157 (m), 1079 (m), 1033 (s), 949 (s), 856 (m), 810 (s), 733 (s), 575 (w), 509 (w).

3. Synthesis of $\text{K}_{23}\text{H}_{15}[(\text{P}_{10}\text{Pd}_{15.5}\text{O}_{50})_2(\gamma\text{-CD})_2]\cdot 120\text{H}_2\text{O}$ (POP-CD)

To a solution of γ -cyclodextrin (0.065 g, 0.050 mmol) in 2 mL 0.5 M KH_2PO_4 solution (pH 7.0), $\text{Pd}(\text{CH}_3\text{COO})_2$ (0.023 g, 0.100 mmol) was added upon stirring. The solution was then stirred at 80 $^{\circ}\text{C}$ and during the first 30 min the pH was kept at 5.3–5.4 by addition of 1 M HNO_3 , and then heating at 80 $^{\circ}\text{C}$ was continued for another 60 min. The turbid dark-red solution was filtered and the filtrate was allowed to evaporate in an open vial at room temperature. The needle-shaped dark-red crystalline product **POP-CD** started to appear after one day and was collected by filtration and air-dried. Yield: 0.014 g (38 % based on Pd). Elemental analysis (%): Calcd: K 8.04, P 5.54, Pd 29.48, C 10.31; Found: K 7.89, P 5.29, Pd 30.29, C 10.13. IR (2% KBr pellet, v/cm^{-1}): 2920 (w), 1635 (s), 1384 (m), 1157 (m), 1080 (m), 1026 (s), 995 (m), 941 (w), 760 (w), 706 (w), 613 (s).

4. Single-Crystal X-ray Diffraction Data

Single crystals of the two compounds, **POT-CD** and **POP-CD**, were mounted in a Hampton cryoloop with *Paratone*[®] N oil cryoprotectant. Data collections were performed at 100 K on a Bruker X8 PROSPECTOR APEX2 CCD diffractometer using Cu $K\alpha$ radiation ($\lambda = 1.54178 \text{ \AA}$).

Data integration and reduction were performed using SaintPlus 6.01.¹ Absorption correction was performed by multi-scan method implemented in SADABS.² Space group was determined using XPREP implemented in APEX2.³ Structure was solved using Direct Methods (SHELXS-97)⁴ and refined using SHELXL-2014⁵ (full-matrix least squares on F^2) contained in WinGX.⁶ Crystal data and refinement conditions for **POT-CD** and **POP-CD** are shown in Table S1.

POT-CD crystal structure was refined as a 2-component twin with the twin law $[-1\ 0\ 0\ 0\ -1\ 0\ 0\ 0\ 1]$ and 0.43% contribution of the second component. Lack of twin refinement results in positive electron density at W atoms. Large set of restraints and constraints was applied to make both geometry and thermal parameters of organic molecules appropriate. Thus, C–C and C–O distances in the α -CD were restrained by DFIX 1.52 0.01 and DFIX 1.43 0.01, respectively. In the case of acetate anion, the corresponding restraints were DFIX 1.5 0.01 and DFIX 1.23 0.01. Thermal parameters of the α -CD molecule atoms were refined with SIMU 0.03, and SIMU 0.01 was applied in the case of acetate anion. ISOR restraints were applied to the O4T, Na3B and oxygen atoms of some water molecules.

Significant disorder in the crystal structure of **POP-CD** caused poor diffraction with significant anisotropy. Large set of restraints and constraints was applied to keep both geometry and thermal parameters of the disordered part of the structure reasonable. DFIX 1.42 0.01, DFIX 1.52 0.01 and DFIX 1.53 0.01 were applied to keep C–O bonds length, length of bonds between two tertiary carbon atoms and length of bonds between the secondary and the tertiary carbon atoms in both γ -CD molecules, respectively. DFIX 2.32, DFIX 2.42 and DFIX 2.52 were applied to keep angles in the glucose moieties reasonable. DFIX -2.43, DFIX -2.72 and DFIX 2.8 were used as 'anti-bumping' restraints. Medium SIMU 0.02 were applied to the thermal parameters of each glucose moiety and standard RIGU 0.005 to each whole γ -CD. ISOR with different values were applied to atoms with large difference between U_{ii}/U_{jj} where atom splitting has no sense. EADP was applied to close located or chemically equivalent atoms. Strongly delocalized electron density was found in voids and excluded from the refinement using the PLATON's SQUEEZE procedure.⁷

In both **POT-CD** and **POP-CD** crystal structures, the organic molecules' hydrogen atoms were placed at calculated positions and refined using the riding model with $U_{iso}(H) = 1.2U_{eq}(C)$. Since was not possible to localize H-atoms of OH-groups and water molecules, as well as whole H₂O molecules (and K⁺ cations in **POP-CD**), the exact number of cations and crystal waters in the compounds was determined by elemental analysis and TGA, so the resulting formula units were further used throughout the paper and in the CIF file for overall consistency.

The crystal data and structure refinement for both compounds are summarized in Table S1. CCDC-1870923 (**POT-CD**) and CCDC-1870924 (**POP-CD**) contain the supplementary crystallographic data for this paper.

5. Battery Analyses

To assess the electrochemical performance, 2032 coin-type (MTI, Inc.) half-cell devices were fabricated. The as-made **POT-CD**, referenced (NBu₄)₃[PW₁₂O₄₀], α -CD, and their stoichiometry mixture (molar ratio of (NBu₄)₃[PW₁₂O₄₀] : α -CD = 1: 1) were used as anode materials to study their respective electrochemical performances in LIBs. By mixing **POT-CD**/(NBu₄)₃[PW₁₂O₄₀]/ α -CD/stoichiometry mixture, Super-P carbon, and polyvinylidene fluoride (PVDF) at a weight ratio of 8:1:1, we obtained the anodes. Then we added

N-methyl-2-pyrrolidinone (NMP) to the mixture to form a paste with appropriate viscosity. The paste was mildly coated on pure Cu foil and vacuum-dried at 50 °C for 24 h. The loading mass of electroactive materials in the electrode slurry is $\sim 1 \text{ mg cm}^{-2}$. Lithium foil was used as the counter and reference electrode, and Celgard 3501 microporous membrane as the separator. 1.0 M LiPF_6 in ethylene carbonate (EC)/diethyl carbonate (DEC) (1/1 in volume) was used as the electrolyte. The coin cells were assembled in an argon-filled glovebox (MBRAUN) with the concentrations of O_2 and $\text{H}_2\text{O} < 0.5 \text{ ppm}$. The electrochemical performance of the assembled cells was measured at different current densities (100–1000 mA/g) in the voltage window from 0.01 to 3.0 V vs. Li/Li^+ using an Arbin battery tester (Arbin BT-2143-11U, College Station, TX, USA). Cyclic voltammetry was performed to examine the reduction and oxidation peaks in the voltage range of 0.01–3.0 V (V vs. Li/Li^+) at a scan rate of $0.1\text{--}0.5 \text{ mV s}^{-1}$ using VMP3 Biologic potentiostat (Biologic, France). Galvanostatic charge-discharge tests were performed at current densities from 0.1 to 1.0 mA cm^{-2} . The electrical impedance spectra (EIS) were measured by applying a sine wave with an amplitude of 5.0 mV over the frequencies 100k–100m Hz.

6. CO_2 Adsorption of POT-CD.

In order to unveil the total or partial porosity of the unstable (under high vacuum) **POT-CD**, a special procedure was developed by using the gravimetric technique coupled to a magnetic suspension balance (MSB) and a gas dosing system combined with a turbo-pump.⁸

The sample was loaded wet (solvent: methanol) in the sample holder, and the solvent was removed from the pore gently for several days:

CO_2 was initially flushed at 298 K for 3 days and after that 5 cycles pressurization-depressurization between 1 and 25 bar were carried out. A baseline material mass was recorded at 298 K and 1 bar and CO_2 adsorption isotherms was collected at 298 K and the recorded uptake was 0.33 mmol/g at 25 bar (Figure S8).

Another adsorption isotherms collection was carried out after flushing CO_2 at 328 K and 1 bar for 1 day. The obtained CO_2 uptake was almost 100% higher than the previous CO_2 adsorption collection (further heating at 85 °C by flushing N_2 led to only a slight increase in CO_2 uptake).

Using the procedure mentioned above, we were able to access an equivalent of $0.03 \text{ cm}^3/\text{g}$ porosity of **POT-CD**.

7. Ex-situ X-ray Photoelectron Spectroscopy (XPS) of POT-CD

Ex-situ XPS experiments were performed to uncover the detailed chemical constituents of SEI and the evolution upon electrochemical cycling. Figure S10a tracks the evolution of O 1s spectrum before and after electrochemical reaction. At the pristine state, there are three peaks at 529.8, 530.8 and 532.0 eV, in which the first peak is characteristic of lattice O^{2-} in the **POT-CD** crystal structure, and the other peaks are related to the weakly adsorbed oxygen species and Li_2CO_3 residuals on the surface.^{9,10} As the XPS gathers only the surface information, here the relative intensity of the oxygen lattice peak may serve as an indicator of the formation of SEI film. When the **POT-CD** anode was first fully discharged, the strong peaks from lattice oxygen (O^{2-}) almost disappeared in intensity while the peaks corresponding to Li_2CO_3 , O-C=O and C=O gained much weight. The decrease in peak intensity can be attributed to the interface reaction and associated SEI formation. When the **POT-CD** anode was further charged to 3.0 eV, the feature from lattice oxygen remained disappearing, which suggests the growth of thick SEI during the charge-discharge process is not reversible.

W 4f XPS shown in Figure S10b was used to deduce the oxidation states of tungsten in the discharge/charge process. The dominant peaks at 37.1 and 35.0 eV of the pristine sample can be assigned to the emission of W 4f_{5/2} and W 4f_{7/2} core levels from the atoms with the W⁶⁺ oxidation state,^{11,12} while the other two weaker peaks located at 35.5 and 33.3 eV correspond to the lower valence of W⁵⁺.^{13,14} When the cell was fully discharged and charged, the change in the relative intensity of W⁵⁺/W⁶⁺ decreased from 31.7% to 9.4%. Hence, we infer that the electrochemical reaction for tungsten is a reversible intercalation pseudocapacitance effect (R-W(+6) + xLi⁺ + xe⁻ ↔ LiW(+5)-R). Pseudocapacitance processes are surface or near surface redox reactions, which is consistent to the significantly increased cycling capacities along with the drastic pulverization process.

8. Electrochemical Performance of POP-CD as Anode Material in LIB

As shown in Figure S19a, the first discharge capacity of the **POP-CD** anode amounts to *ca.* 565 mAh/g, and the charge capacity is *ca.* 245 mAh/g, resulting in an initial coulombic efficiency of 43 %. The irreversible capacity loss results principally from the decomposition of the electrolyte and subsequent formation of the SEI film. In the subsequent cycling stability test, the capacities gradually decreased and remained stable at *ca.* 85 mAh/g over 80 cycles (Figure S19b).

In sharp contrast to the **POT-CD** anode, of which the cycling capacity rose up as a function of cycle numbers (695 mAh/g at the 450th cycle), the lower capacity of **POP-CD** could be mainly attributed to the irreversible multielectron redox behavior of the POP units. Based on the previous research, the cyclic voltammetry proved that the reduction of POPs could irrevocably result in the deposition of a Pd⁰ film and consequently the loss of the electron storage function as anode material in LIB.¹⁵

9. FT-IR Spectra of POT-CD and POP-CD.

FT-IR spectra recorded on both compounds are presented in Figures S26 and S27. For both spectra, the strong absorption peak of O–H bonds of cyclodextrins is located at ~3400 cm⁻¹. The band centered at ~2920 cm⁻¹ belongs to the asymmetrical stretching vibration of C–H bonds while the band at ~1650 cm⁻¹ originates from the C–C stretching of polysaccharides. The peaks occur in the region from 1480 to 1180 cm⁻¹ correspond to the C–H bending vibrations while the band located between 1160 – 1040 cm⁻¹ is characteristic of the symmetrical stretching of glycosidic C–O–C and C–O bonds in polysaccharides.¹⁶

For **POT-CD**, a characteristic absorption band centered at 1076 cm⁻¹ is typical for P–O bonds. The peaks that are below 1000 cm⁻¹ can be designated to the terminal W=O bonds as well as the bridging W–O–W bond stretching modes.¹⁷ For **POP-CD**, intense absorption bands that correspond to different vibrational modes of Pd–O groups appear in the region between 767 – 605 cm⁻¹. In addition, absorption peaks at 1076 and 991 cm⁻¹ are attributed to the phosphate heterogroups.

Table S1. Crystal data and structure refinement for **POT-CD** and **POP-CD**

	POT-CD	POP-CD
Empirical formula	C ₃₈ H ₁₀₂ K _{2.5} Na _{2.5} O ₉₂ PW ₁₂	C ₉₆ H ₄₁₅ K ₂₃ O ₃₀₀ P ₂₀ Pd ₃₁
Formula weight	4423.58	11188.36
Crystal system, space group	Monoclinic, <i>P</i> 2 ₁	Orthorhombic, <i>P</i> 2 ₁ 2 ₁ 2 ₁
Unit cell dimensions	<i>a</i> = 16.7418(8) Å, <i>b</i> = 15.6598(8) Å, <i>β</i> = 90.376(2)° <i>c</i> = 18.4127(9) Å	<i>a</i> = 13.5988(8) Å, <i>b</i> = 47.708(3) Å, <i>c</i> = 50.646(3) Å
Volume	4827.2(4) Å ³	32858(3) Å ³
<i>Z</i> , calculated density	2, 3.043 Mg m ⁻³	4, 2.262 Mg m ⁻³
<i>F</i> (000)	4088	22216
Temperature (K)	100.0(1)	100.0(1)
Radiation type, <i>λ</i>	Cu <i>Kα</i> , 1.54178 Å	Cu <i>Kα</i> , 1.54178 Å
Absorption coefficient	28.06 mm ⁻¹	18.08 mm ⁻¹
Absorption correction	Multi-scan	Multi-scan
Max and min transmission	0.149 and 0.047	0.753 and 0.468
Crystal size	0.12 × 0.16 × 0.18 mm	0.16 × 0.28 × 0.32 mm
Shape, colour	Prism, colorless	Prism, red
<i>θ</i> range for data collection	2.4–66.7°	2.0–57.9°
Limiting indices	-19 ≤ <i>h</i> ≤ 19, -18 ≤ <i>k</i> ≤ 16, -21 ≤ <i>l</i> ≤ 21	-14 ≤ <i>h</i> ≤ 14, -52 ≤ <i>k</i> ≤ 52, -53 ≤ <i>l</i> ≤ 54
Reflection collected / unique / observed with <i>I</i> > 2σ(<i>I</i>)	67495 / 16220 (<i>R</i> _{int} = 0.053) / 14853	127994 / 43246 (<i>R</i> _{int} = 0.068) / 39444
Completeness to <i>θ</i> _{max}	99.2 %, 62.4°	96.6 %, 57.9°
Refinement method	Full-matrix least-squares on <i>F</i> ²	Full-matrix least-squares on <i>F</i> ²
Data / restraints / parameters	16220 / 617 / 1308	43246 / 3042 / 3713
Final <i>R</i> indices [<i>I</i> > 2σ(<i>I</i>)]	<i>R</i> ₁ = 0.063, <i>wR</i> ₂ = 0.201	<i>R</i> ₁ = 0.077, <i>wR</i> ₂ = 0.216
Final <i>R</i> indices (all data)	<i>R</i> ₁ = 0.067, <i>wR</i> ₂ = 0.205	<i>R</i> ₁ = 0.082, <i>wR</i> ₂ = 0.222
Weighting scheme	[σ ² (<i>F</i> _o ²) + (0.1441 <i>P</i>) ² + 36.7151 <i>P</i>] ⁻¹ *	[σ ² (<i>F</i> _o ²) + (0.1387 <i>P</i>) ² + 305.2558 <i>P</i>] ⁻¹ *
Goodness-of-fit	1.07	1.03
Largest diff. peak and hole	4.12 and -3.88 e Å ⁻³	4.07 and -1.86 e Å ⁻³

$$*P = (F_o^2 + 2F_c^2)/3$$

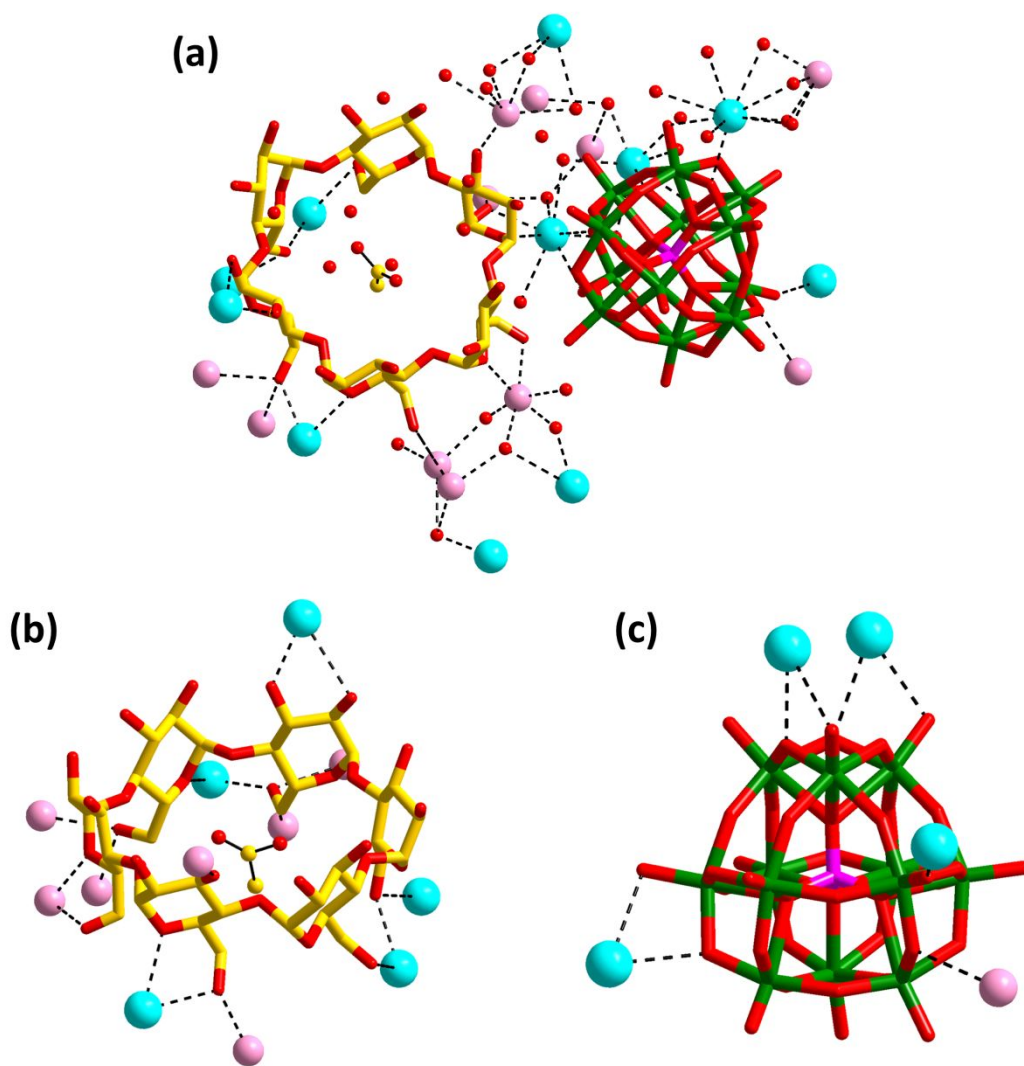


Figure S1. a) The asymmetric unit of **POT-CD**. Hydrogen atoms and lattice water molecules are omitted for clarity. b) The coordination environment of α -CD in **POT-CD**. c) The coordination environment of PW_{12} in **POT-CD**. Color code: W, green; P, pink; K, turquoise; Na, magenta; O, red; C, yellow.

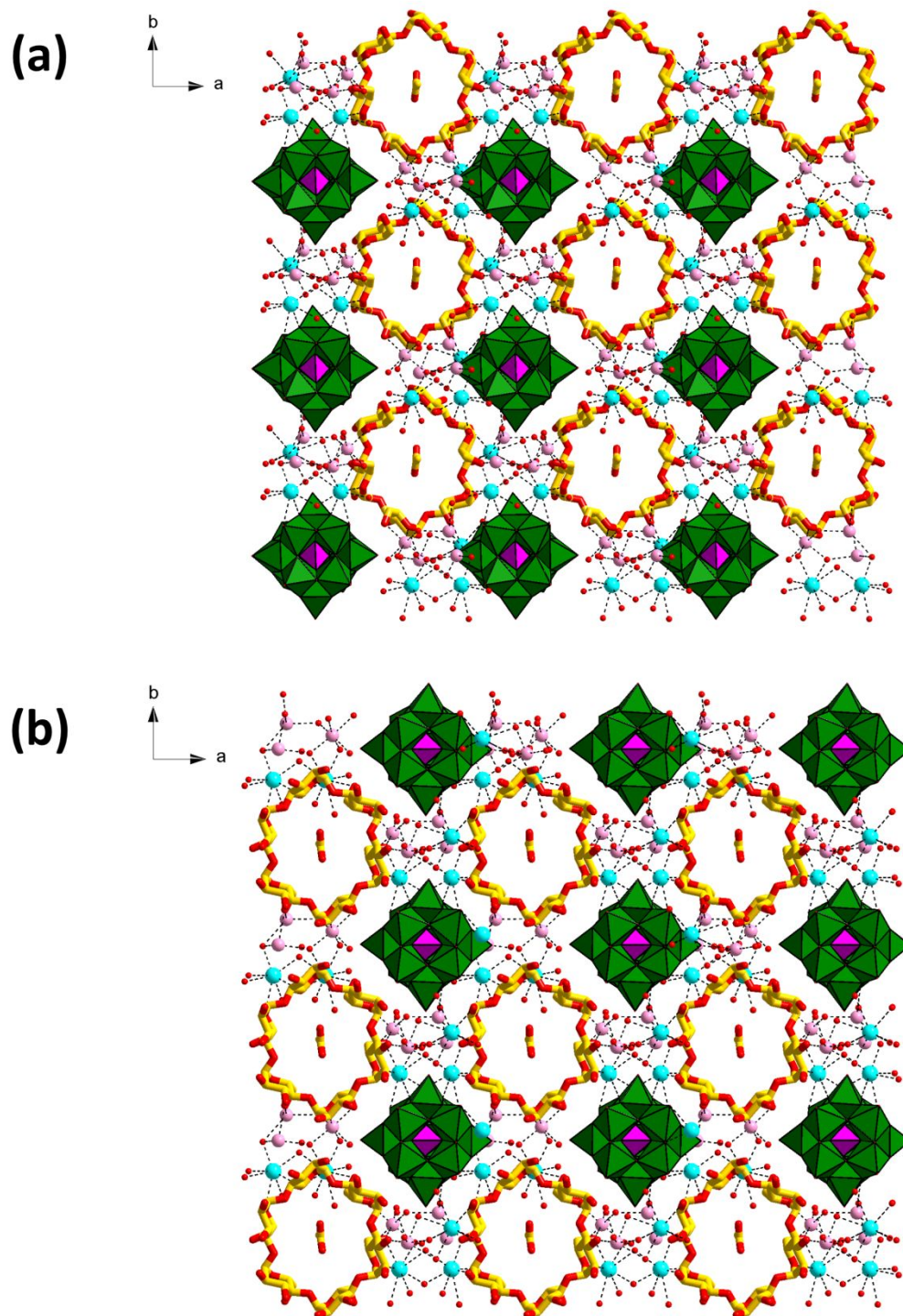


Figure S2. Perspective views of layer A (a) and layer B (b) in **POT-CD** along the c axis. Color code same as Figure 1a.

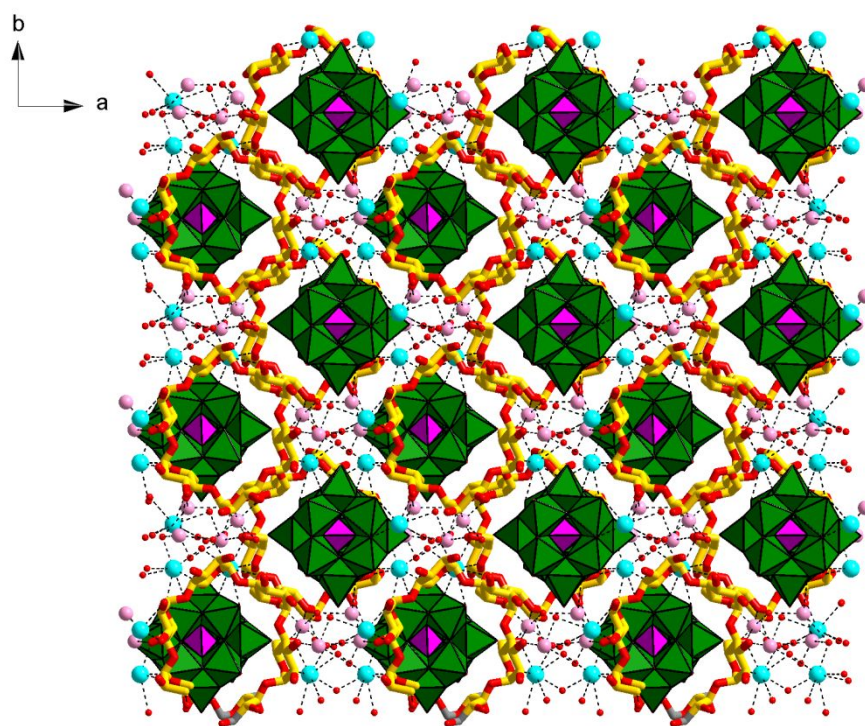


Figure S3. Perspective view of **POT-CD** along the c axis. Color code same as Figure 1a.

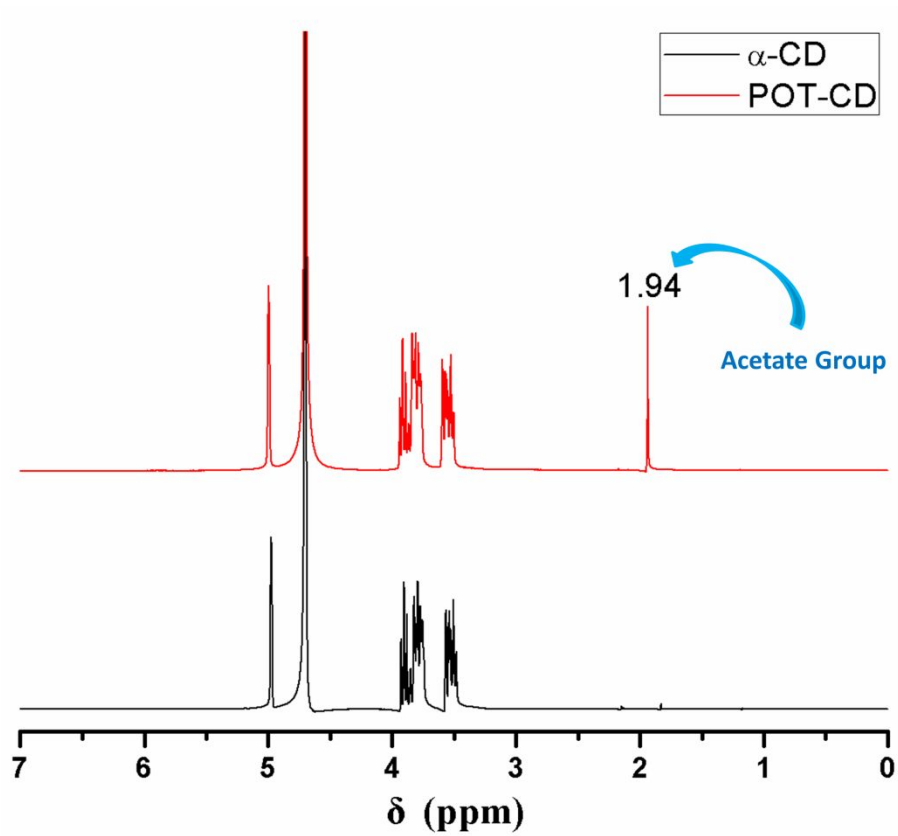


Figure S4. ^1H NMR spectra of **POT-CD** and α -CD recorded in D_2O at room temperature.

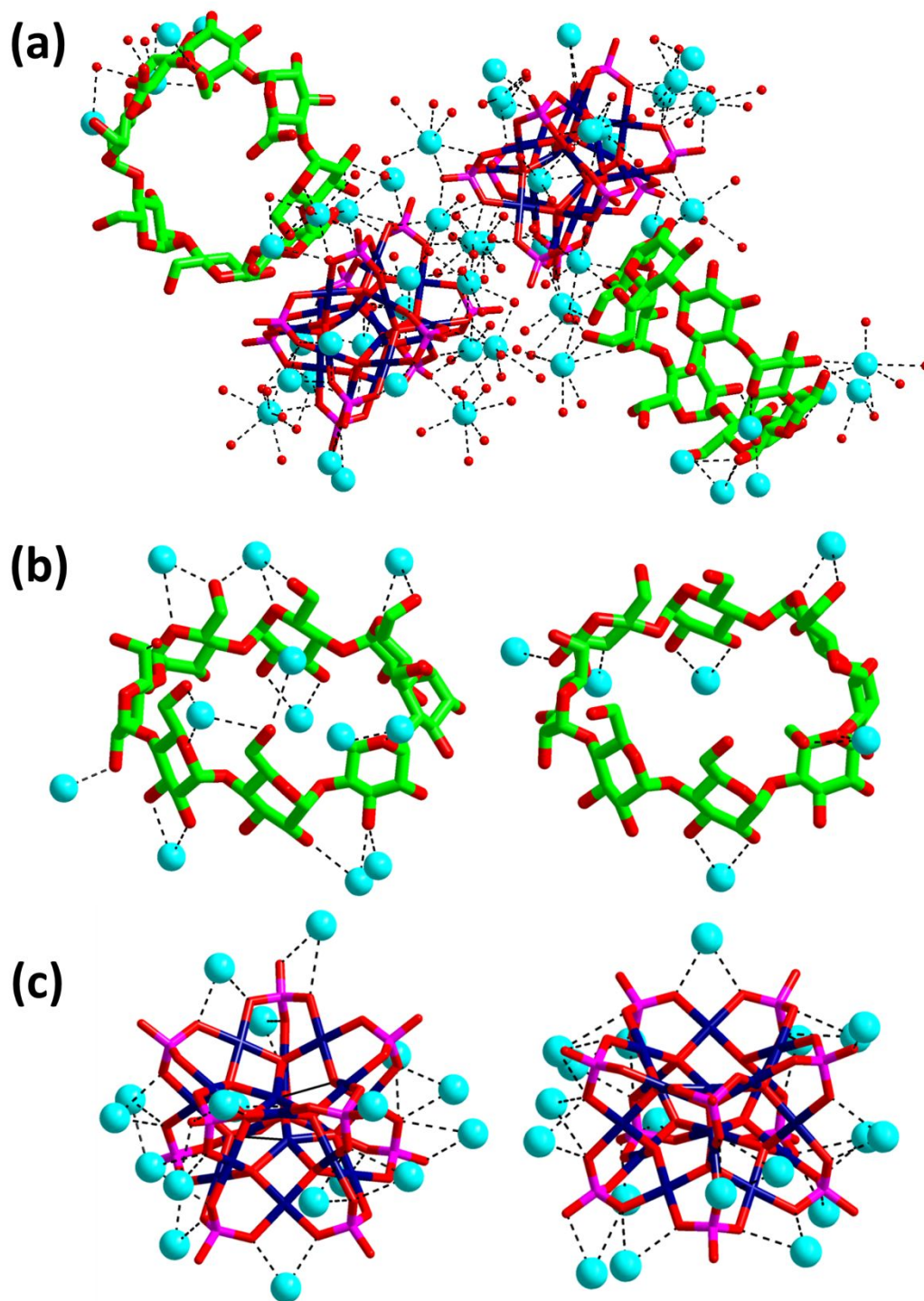


Figure S5. a) The asymmetric unit of **POP-CD**. Hydrogen atoms and lattice water molecules are omitted for clarity. b) The coordination environment of γ -CDs in **POP-CD**. c) The coordination environment of $P_{10}Pd_{15.5}$ in **POP-CD**. Color code: Pd, blue; P, pink; K, turquoise; O, red; C, green.

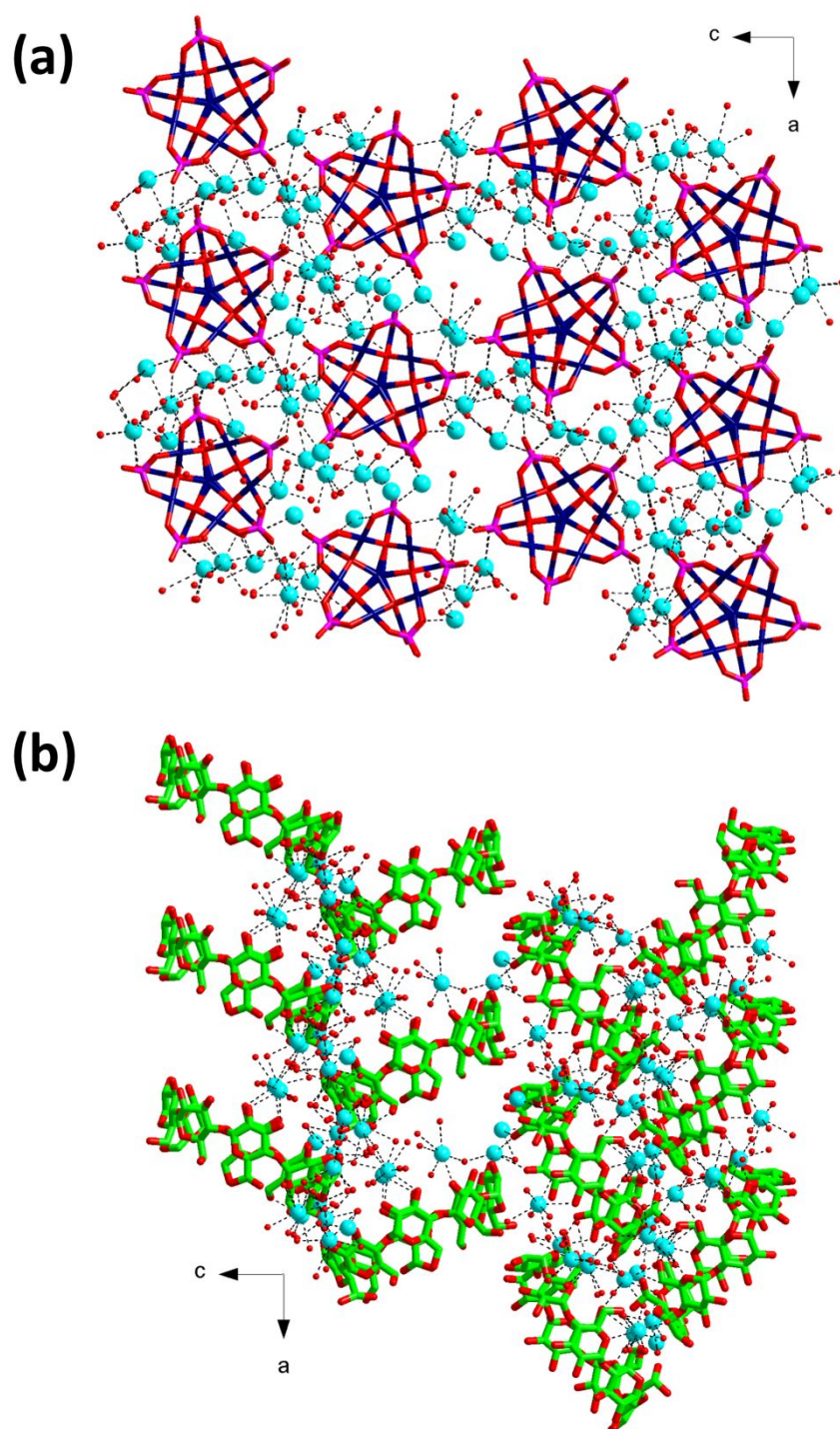


Figure S6. Perspective views of layer POP (a) and layer CD (b) in **POP-CD** along the b axis. Color code same as Figure S5.

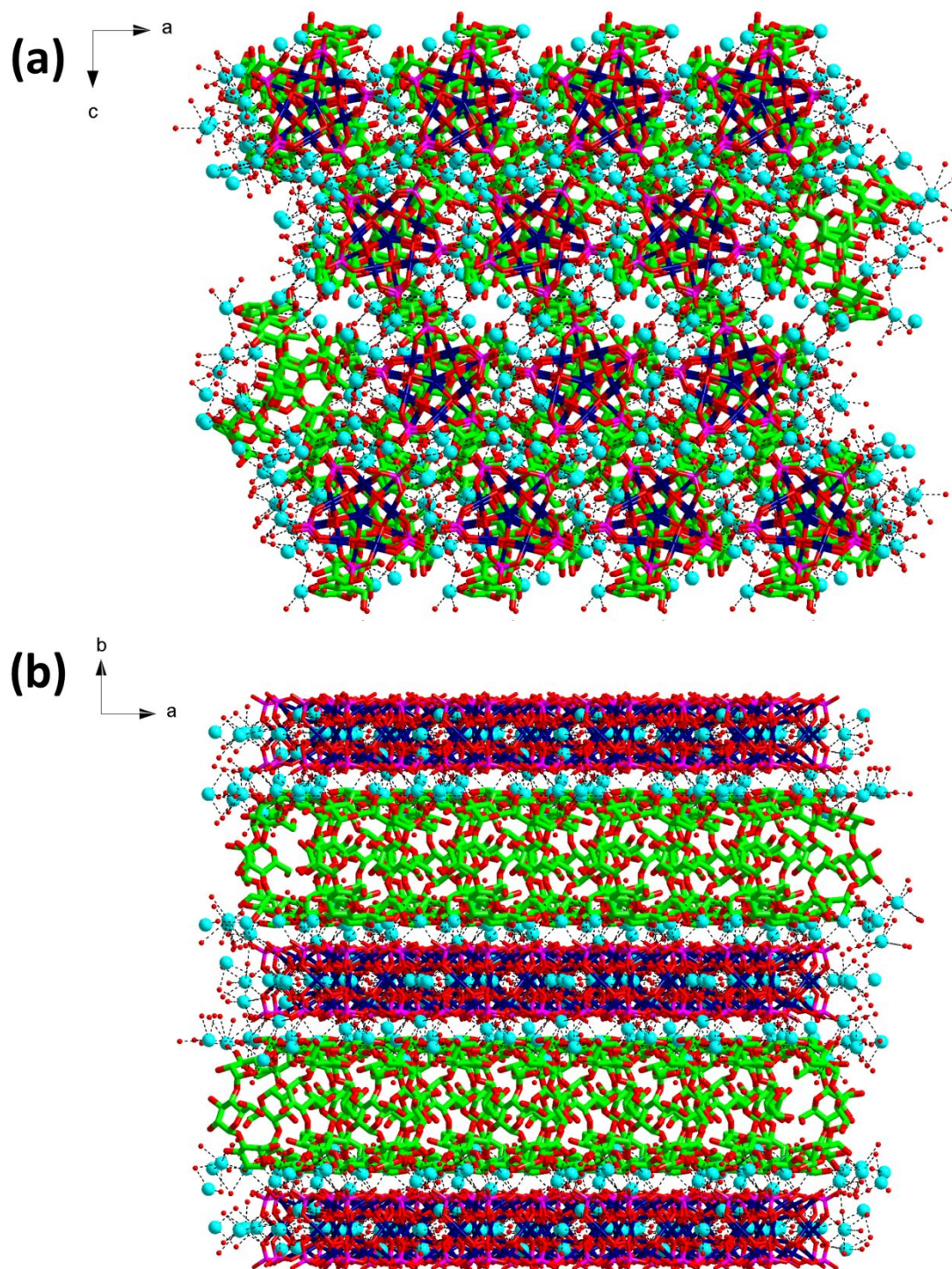


Figure S7. Perspective views of **POP-CD** along the b (a) and c (b) axes. Color code same as Figure S5.

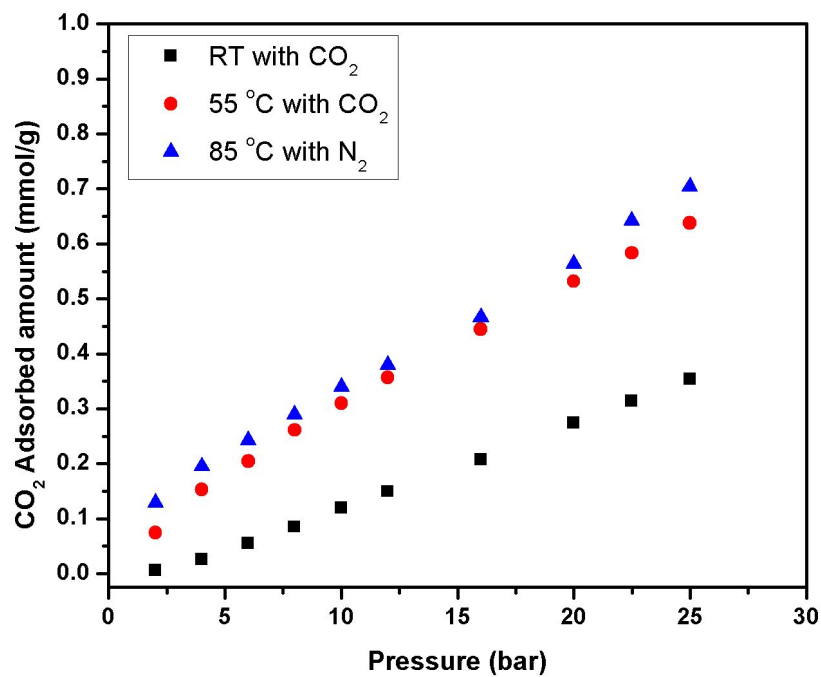


Figure S8. CO₂ sorption for **POT-CD** under different activation conditions.

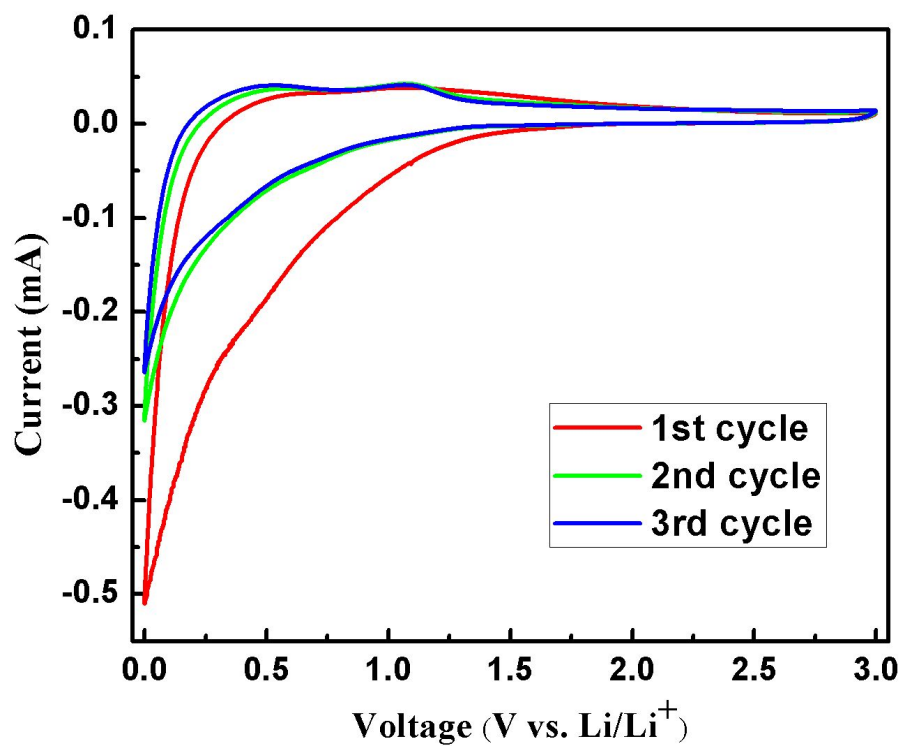


Figure S9. Cyclic voltammograms of the **POT-CD** anode recorded at a scan rate of 0.1 mV s⁻¹ in the potential range of 0.01–3.0 V.

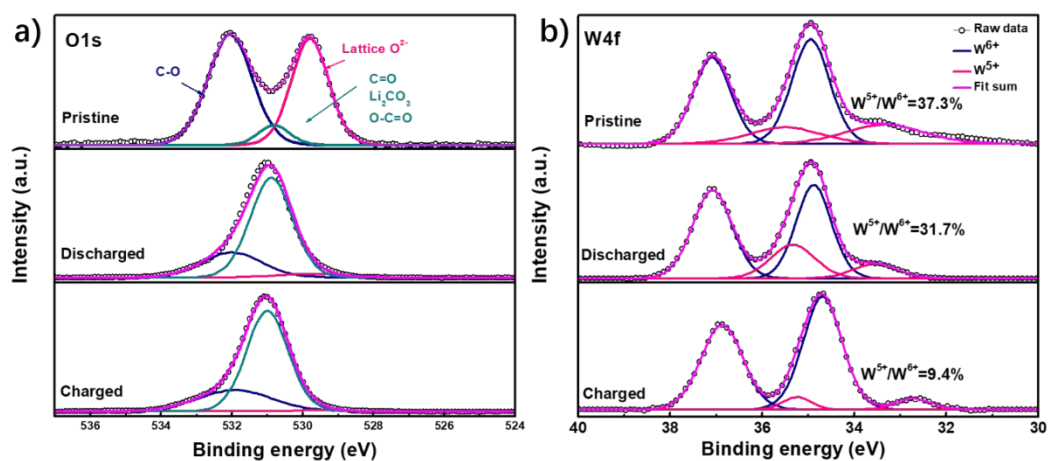


Figure S10. (a) Evolution of O 1s XPS and (b) W 4f XPS of **POT-CD** anodes at different charge and discharge states. The black circles are the experimental data and the magenta curve is the summation of the decomposed curves.

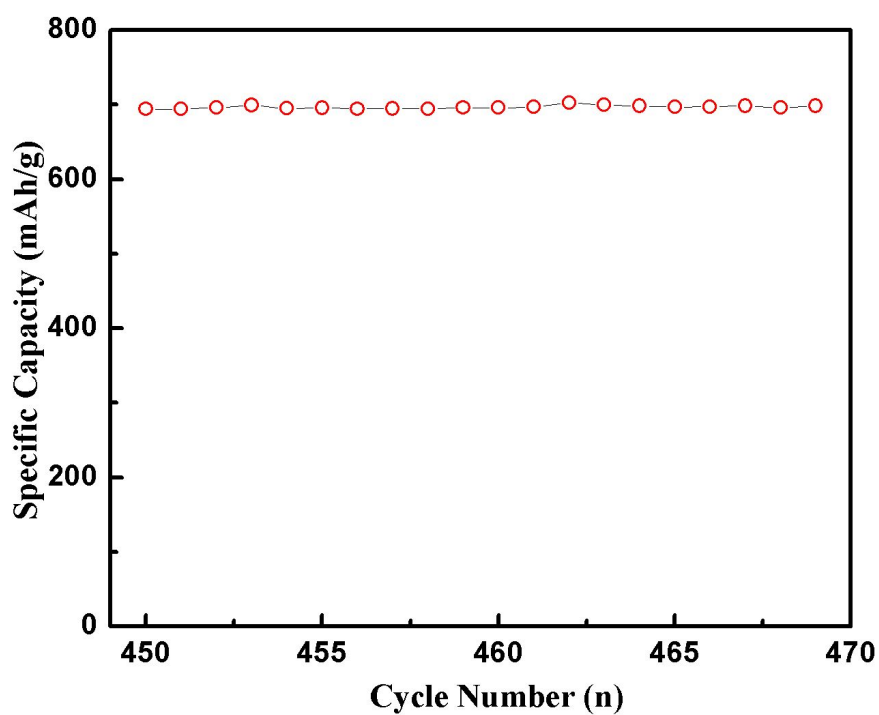


Figure S11. Discharge capacities of the **POT-CD** anode for LIB from 450 to 470 cycles at a current density of 100 mA/g.

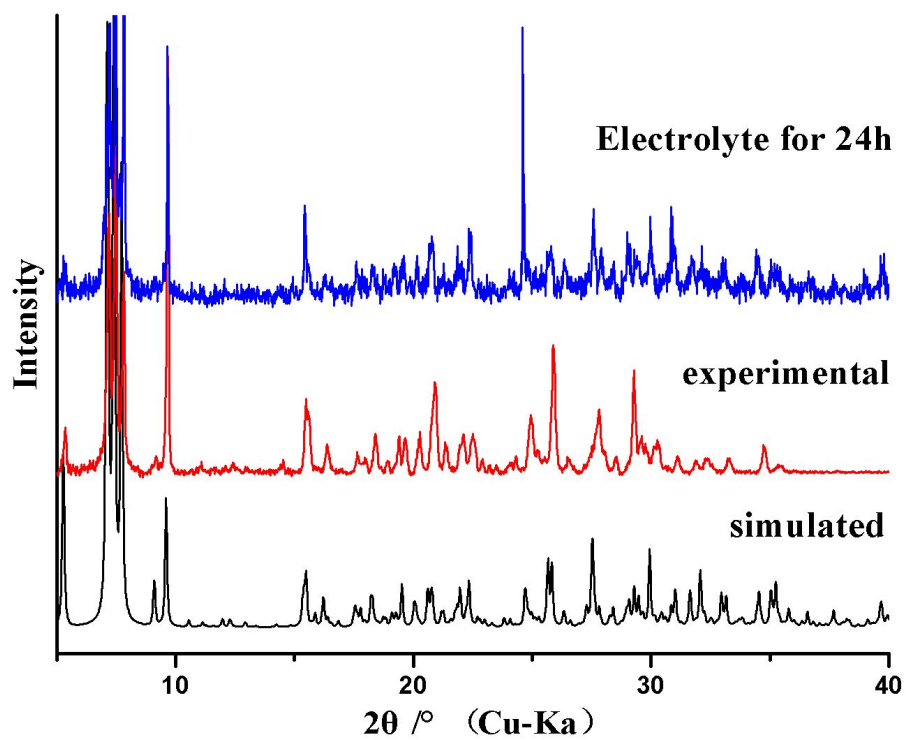


Figure S12. PXRD patterns of **POT-CD**.

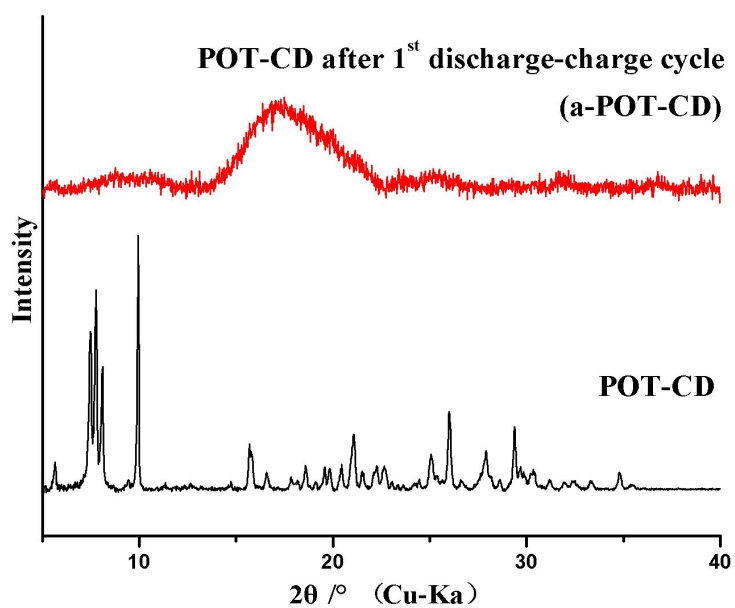


Figure S13. PXRD patterns of **POT-CD** and **a-POT-CD**.

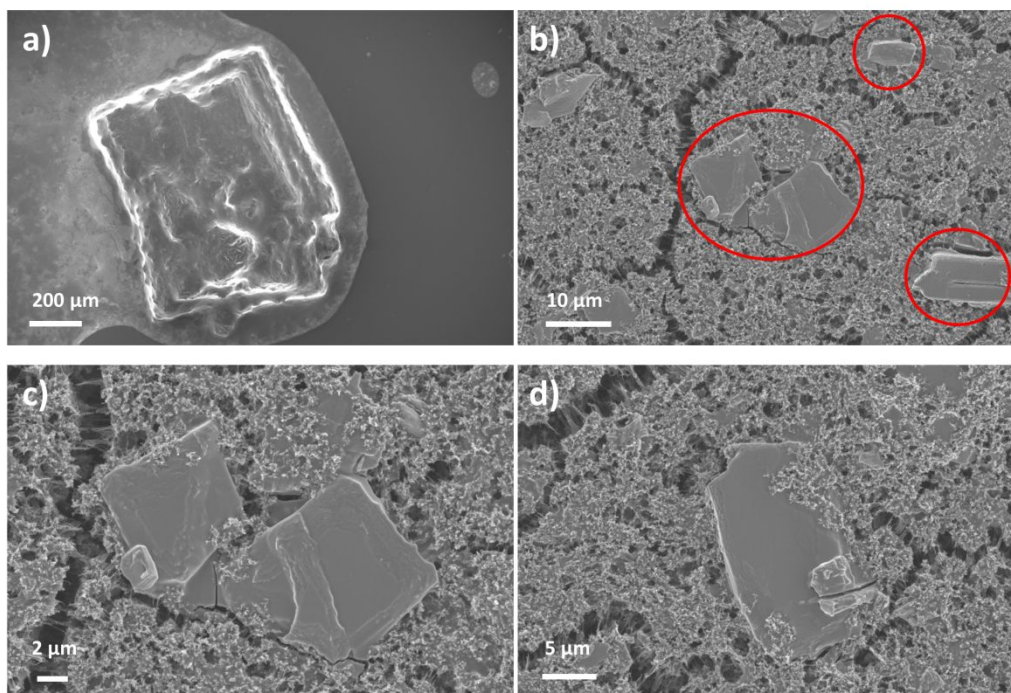


Figure S14. (a) SEM image of **POT-CD** crystal. (b) SEM image of the pristine **POT-CD** anode (after grinding) on Cu foil infiltrated with Super-P carbon and PVDF. (c,d) magnified SEM images showing the morphology of the **POT-CD** anode.

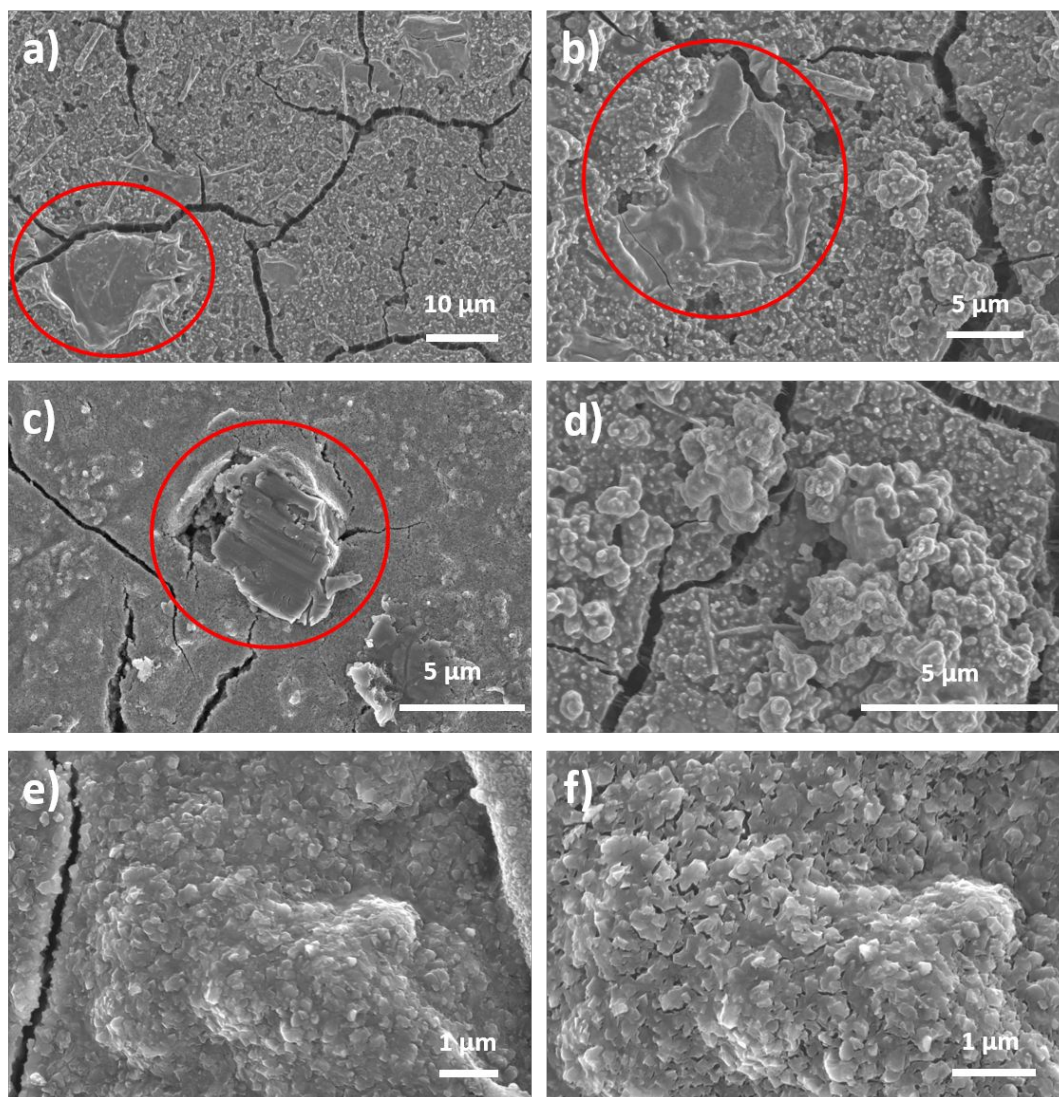


Figure S15. SEM images of **POT-CD** anodes after 1 discharge-charge cycle (a), 10 cycles (b), 50 cycles (c), 100 cycles (d), 150 cycles (e), 200 cycles (f).

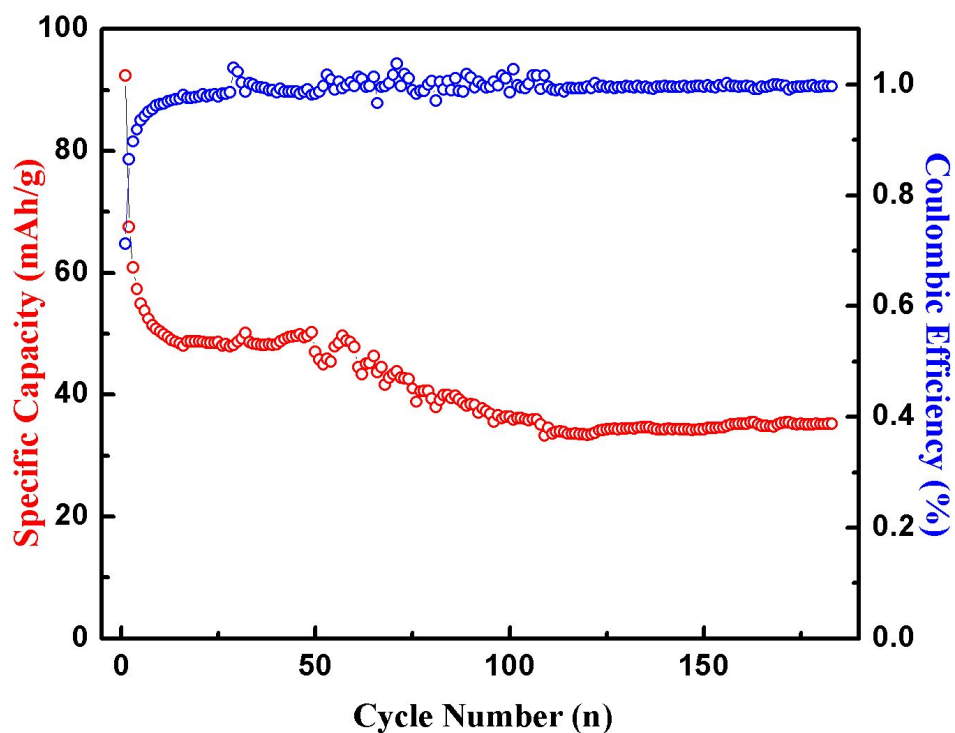


Figure S16. Cycling performance and coulombic efficiencies of the $(\text{NBu}_4)_3[\text{PW}_{12}\text{O}_{40}]$ referenced anode at 100 mA/g. The specific capacity was calculated based on the mass of active material.

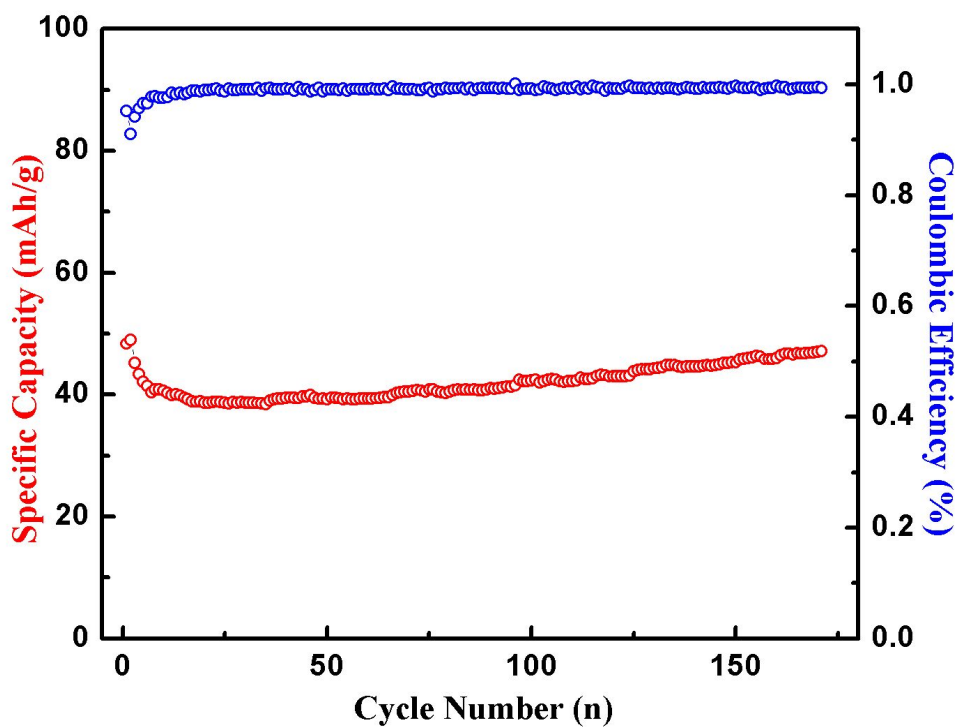


Figure S17. Cycling performance and coulombic efficiencies of the α -CD referenced anode at 100 mA/g. The specific capacity was calculated based on the mass of active material.

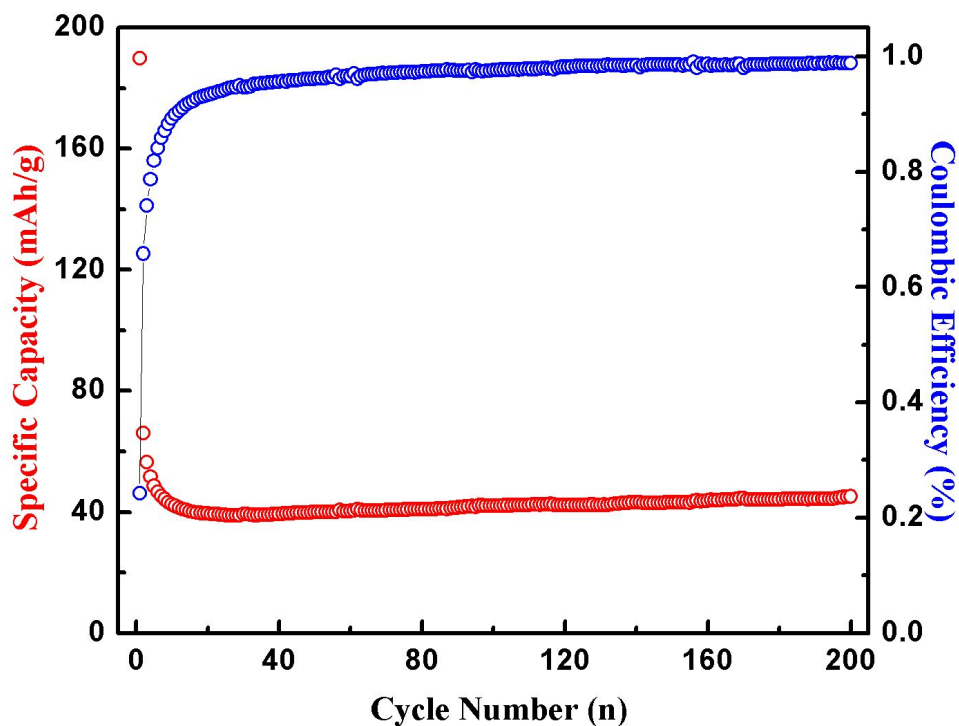


Figure S18. Cycling performance and coulombic efficiencies of the referenced anode ($\text{PW}_{12} : \alpha\text{-CD} = 1 : 1$) at 200 mA/g. The specific capacity was calculated based on the mass of active material.

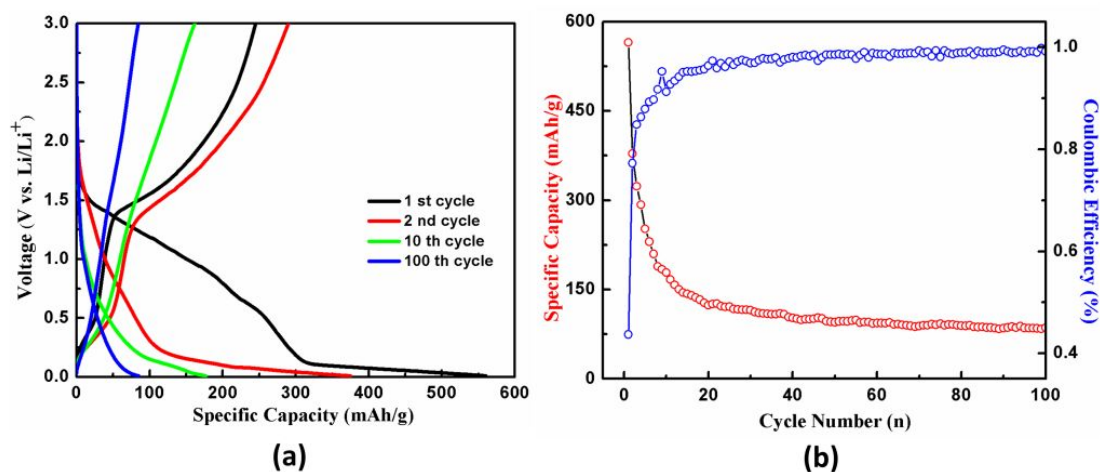


Figure S19. (a) Charge-discharge curves for different cycles at 100 mA/g. (b) Cycling performance and coulombic efficiencies at 100 mA/g. The specific capacity of the **POP-CD** anode was calculated based on the mass of active material.

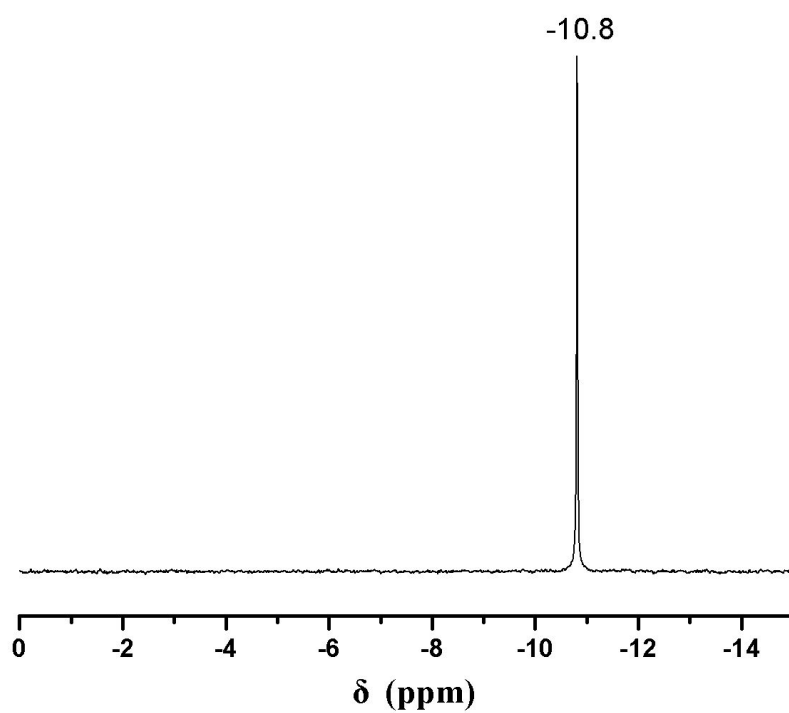


Figure S20. ^{31}P NMR spectrum of **POT-CD** recorded in D_2O at room temperature.

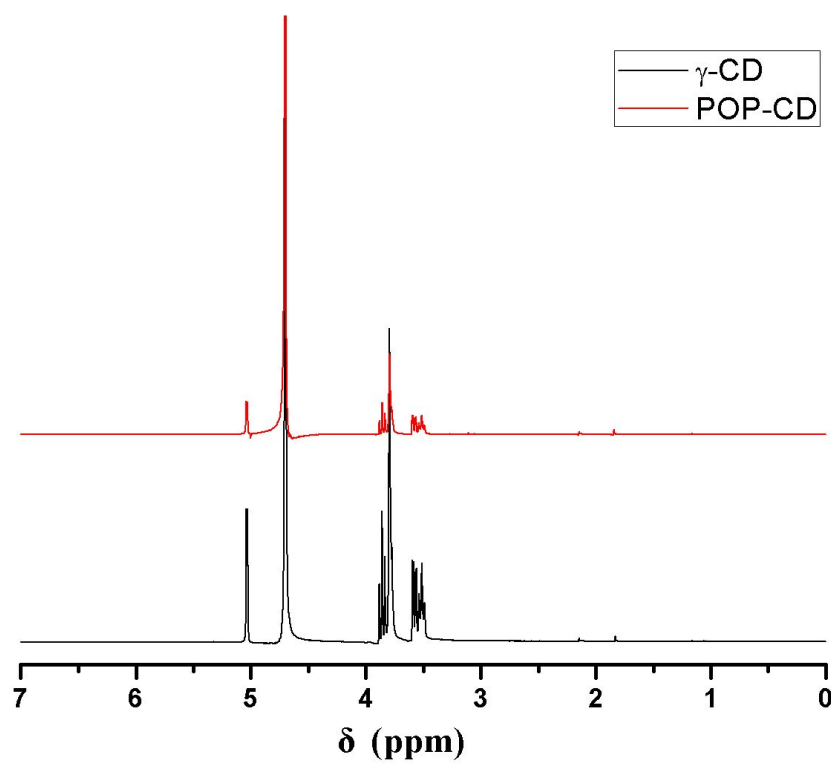


Figure S21. ^1H NMR spectra of **POP-CD** and γ -CD recorded in D_2O at room temperature.

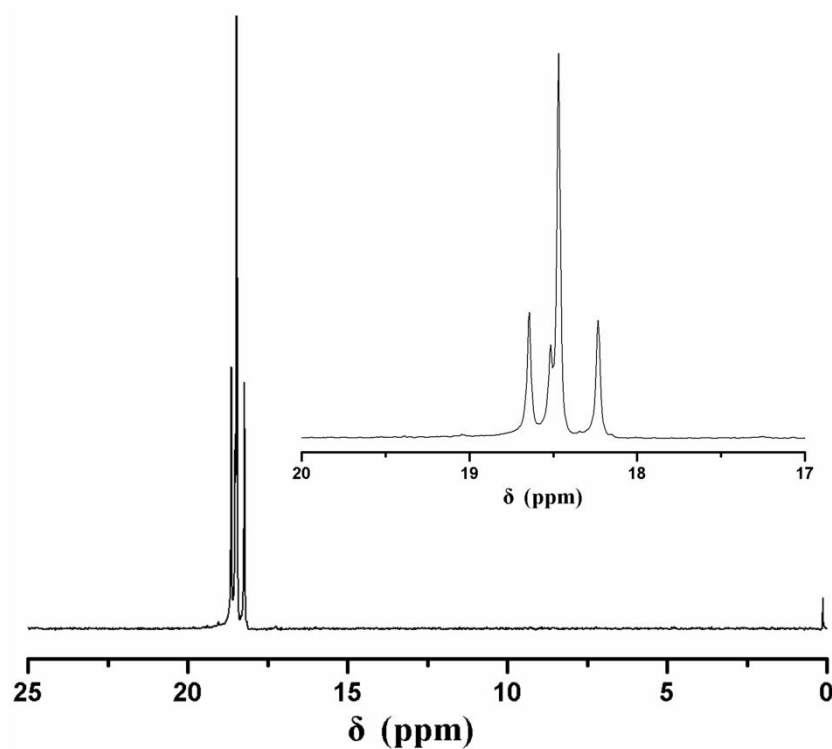


Figure S22. ^{31}P NMR spectrum of **POP-CD** recorded in D_2O at room temperature.

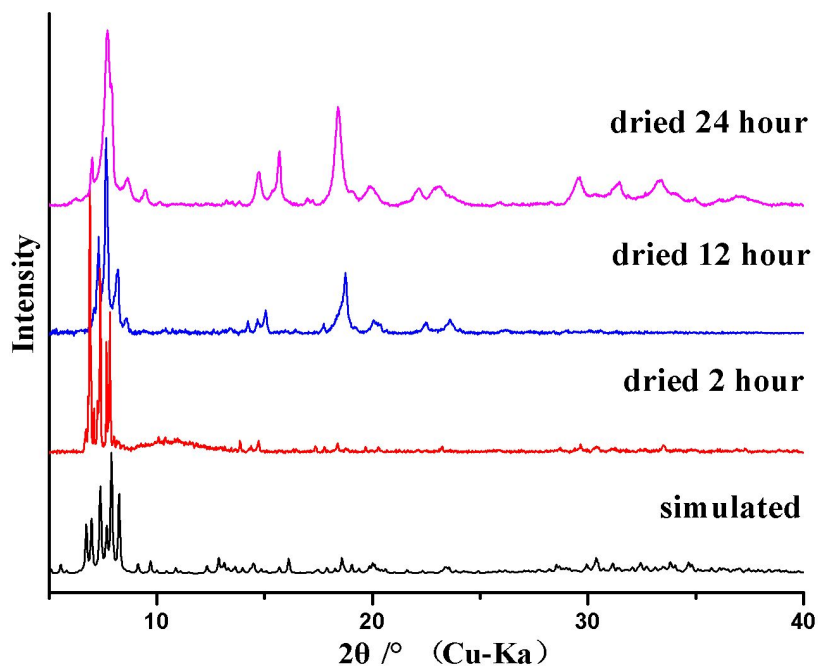


Figure S23. PXRD patterns of **POP-CD**. As a function of drying time, the shifted PXRD patterns confirm a gradual weathered process of **POP-CD** indicating its sensitivity to the evaporation of crystal water molecules. The intensity dissimilarity is due to the different orientations of the powder sample during measurements.

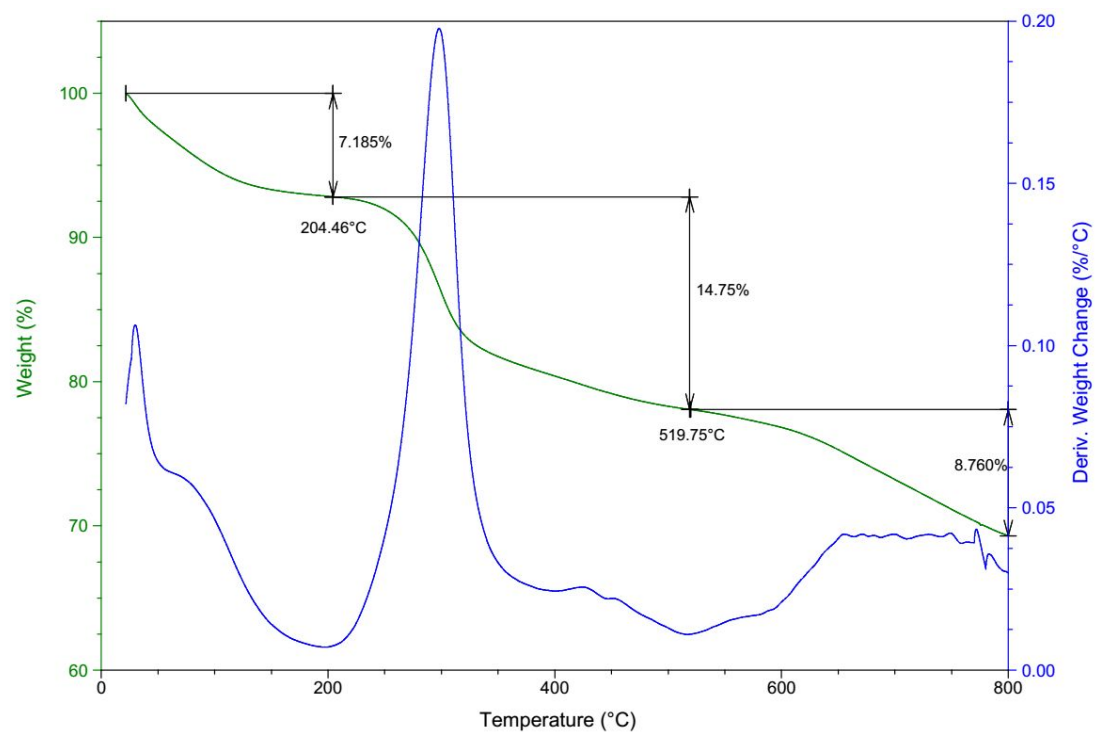


Figure S24. Thermogram of **POT-CD** from 20 to 800 °C under N₂ atmosphere.

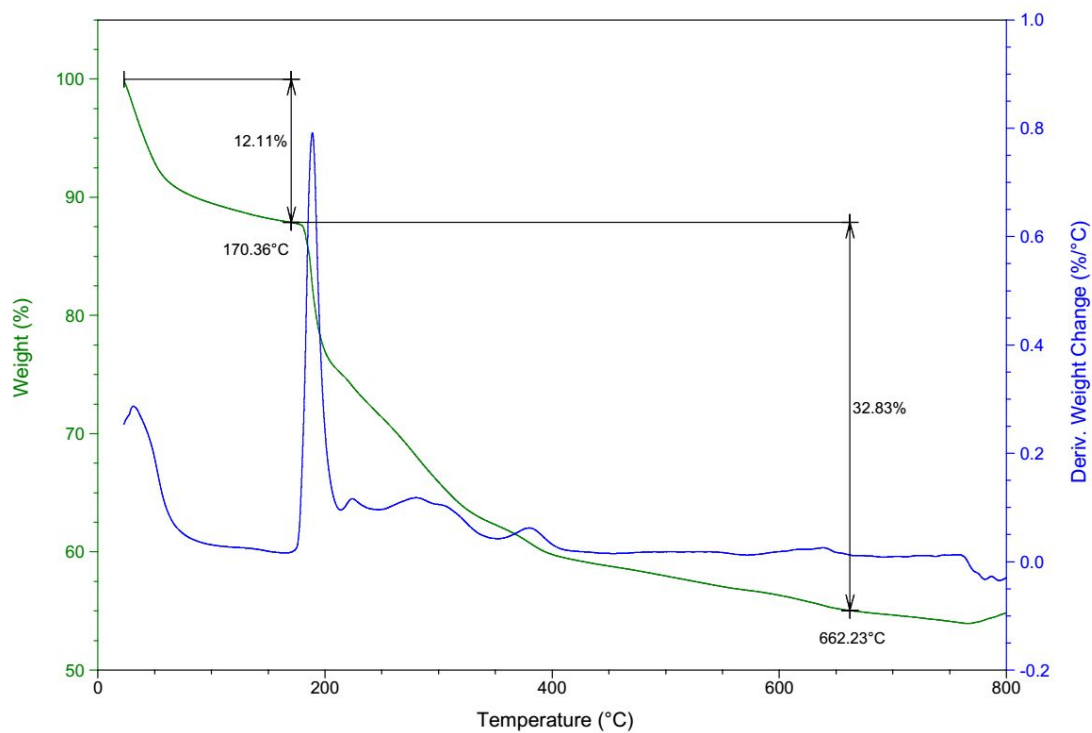


Figure S25. Thermogram of **POP-CD** from 20 to 800 °C under N₂ atmosphere.

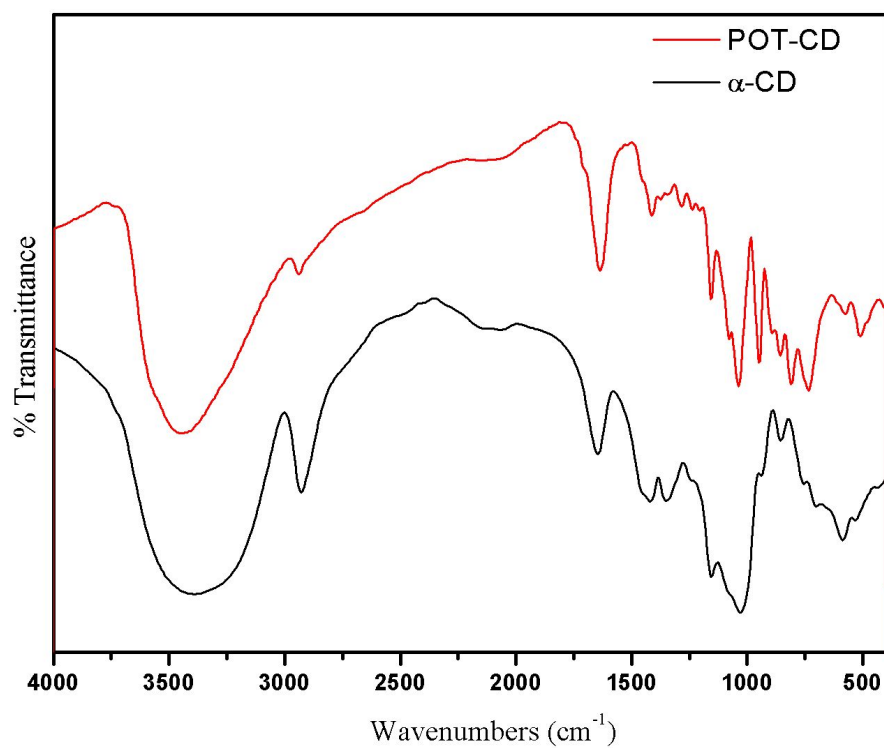


Figure S26. FT-IR spectra of **POT-CD** and α -CD.

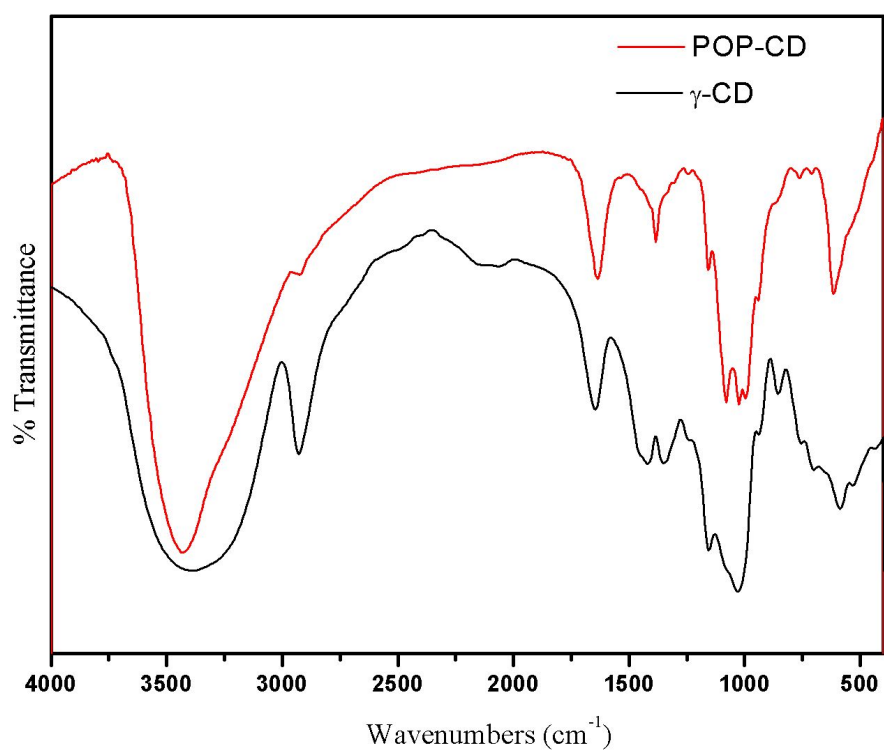


Figure S27. FT-IR spectra of **POP-CD** and γ -CD.

References

1. *SAINT*, Area-Detector Integration Software. Bruker AXS. Inc, Madison, Wisconsin, USA, 2014.
2. Sheldrick, G. M. *SADABS*, Program for empirical X-ray absorption correction, Bruker-Nonius, 2008.
3. *APEX2*. Bruker AXS Inc, Madison, Wisconsin, USA, 2014.
4. Sheldrick, G. M. *SHELXS-97*, Program for Crystal Structure Solution and Refinement, University of Göttingen, 1997.
5. Sheldrick, G. M. *Acta Cryst.* **2015**, *C71*, 3–8.
6. WinGX. Farrugia, L. J. *J. Appl. Cryst.* **2012**, *45*, 849–854.
7. Spek, A. L. *Acta Cryst.* **2009**, *D65*, 148–155.
8. Belmabkhout, Y.; Serna-Guerrero, R.; Sayari, A. *Adsorption* **2011**, *17*, 395–401.
9. Yuan, S.; Liu, Y.-B.; Xu, D.; Ma, D.-L.; Wang, S.; Yang, X.-H.; Cao, Z.-Y.; Zhang, X.-B. *Adv. Sci.* **2015**, *2*, 1400018.
10. Liu, T.; Lin, L.; Bi, X.; Tian, L.; Yang, K.; Liu, J.; Li, M.; Chen, Z.; Lu, J.; Amine, K.; Xu, K.; Pan, F. *Nat. Nanotechnol.* **2018**, DOI: 10.1038/s41565-018-0284-y.
11. Wang, H.; Hamanaka, S.; Nishimoto, Y.; Irle, S.; Yokoyama, T.; Yoshikawa, H.; Awaga, K. *J. Am. Chem. Soc.* **2012**, *134*, 4918–4924.
12. Genovese, M.; Foong, Y. W.; Lian, K. *Electrochim. Acta* **2016**, *199*, 261–269.
13. Nishimoto, Y.; Yokogawa, D.; Yoshikawa, H.; Awaga K.; Irle, S. *J. Am. Chem. Soc.* **2014**, *136*, 9042–9052.
14. Wang, S.; Li, H.; Li, S.; Liu, F.; Wu, D.; Feng, X.; Wu, L. *Chem. -Eur. J.* **2013**, *19*, 10895–10902.
15. Izarova, N. V.; Ngo Biboum, R.; Keita, B.; Mifsud, M.; Arends, I. W. C. E.; Jameson, G. B.; Kortz, U. *Dalton Trans.* **2009**, *43*, 9385–9387.
16. Socrates, G. *Infrared and Raman Characteristic Group Frequencies*, John Wiley & Sons Ltd, United Kingdom, 3rd edn, 2001.
17. Rocchiccioli-Deltcheff, C.; Fournier, M.; Franck, R.; Thouvenot, R. *Inorg. Chem.* **1983**, *22*, 207–216.